Electron-ion equilibration in a strongly coupled plasma

A. Ng, P. Celliers,* G. Xu, and A. Forsman
Department of Physics, University of British Columbia, Vancouver, British Columbia, Canada V6T 1Z1
(Received 31 October 1994; revised manuscript received 27 April 1995)

A recent study on the optical emission from a shock front in flight in silicon has revealed significant deviations of the shock-produced state from thermodynamic equilibrium. The findings also yielded an estimate of the rate of energy equilibration between electrons and ions in a plasma above solid densities, providing important insight into the transport properties of a strongly coupled plasma. Highlights of this study have been reported earlier. Here, we present a detailed account of the theoretical calculation, the experimental measurement, and the interpretation of the results.

PACS number(s): 52.25.Fi, 52.25.Rv, 52.35.Tc

I. INTRODUCTION

Strongly coupled plasmas exist in many laboratory and natural phenomena including inertial confinement fusion, shock or radiation heating of solids, exploding wires, capillary discharges, hypervelocity impacts, Jovian planets, and stellar interiors. These states are dominated by strong particle correlation effects. They cannot be treated simply as periodic structures like a solid lattice; nor can they be described solely by the statistical behavior of a screened Coulomb system as in the case of a rarefied plasma. However, many intriguing questions arise with such states. Recent studies have focused on the conductivity minimum [1–6], shifts in core atomic levels [7,8], as well as the electron-ion equilibration rate [9].

The rate of energy equilibration between electrons and ions is of particular interest since it plays an important role not only in plasma physics but also in shock physics. In a shock wave, the thermal energy at the shock front is carried initially by the ions and the electrons are heated subsequently via electron-ion collisions. The finite rate of energy exchange between the two species leads to a nonequilibrium region immediately behind the shock front. This has been observed in a measurement of the intensity of optical emission from a shock wave in silicon. The observed brightness temperature was significantly below that expected for a shock wave in thermal equilibrium. The results suggested that at the shock front, the electron temperature was substantially less than the ion temperature. The analysis also leads to an estimate of the electron-ion coupling constant which governs energy equilibration. Highlights of this investigation have been reported earlier [9]. In this paper, we will present a more detailed account of the theoretical model (Sec. II), the experiment (Sec. III), the interpretation of the shock emission data (Sec. IV), together with some further discussions (Sec. V), and conclusions (Sec. VI).

*Present address: Lawrence Livermore National Laboratory, Livermore, CA 94550.

II. THEORETICAL MODEL

In the experiment, the shock wave is produced in a silicon wafer by laser-driven ablation and the optical emission from the shock front is recorded before it reaches the free (rear) surface of the target. In modeling the experiment using a hydrodynamic code, high spatial resolution is required both to treat the laser absorption and ablation processes, as well as to compute the optical emission from the shock front. An efficient way to meet this requirement is to model the shock generation and emission problems separately instead of increasing significantly the number of spatial grid points or rezoning the shock front in the emission calculation. This prescription is acceptable since the shock can be considered as a steady wave in the duration of the emission measurement.

The hydrodynamic code used here solves the one-dimensional fluid equations in a Lagrangian formalism. The target material is regarded as a compressible fluid composed of electrons and ions with equal or unequal temperatures. In addition, a radiation field corresponding to the incident laser pulse interacts with the material through the classical inverse bremsstrahlung absorption. General aspects of the code have been described in detail elsewhere [10]. The following discussions will focus on the more specific theoretical issues.

A. Equation of state of silicon

Equation of state is a critical element in the model as it determines the thermodynamic properties of the material. Silicon displays a rich variety of phase transitions at elevated pressures. These have been investigated since the pioneering work of Minomura and Drickamer [11]. The sequence of phase transitions include cubic diamond to body-center tetragonal at 11 GPa [12], to simple hexagonal at 13–16 GPa [13], to an intermediate phase of undetermined structure at 34 GPa, to hexagonal-close packed above 40 GPa [14], and to face-center cubic above 78 GPa [15]. Silicon also becomes metallic at 12 GPa [11]. Since these phase transitions occur at pressures substantially below the shock pressure of interest and since we are primarily concerned with macroscopic parameters

such as shock speed and temperature, the equation of state required has to give a reasonably accurate description of the high-pressure Hugoniot properties of the material only. The most dominant effect of the sequence of phase changes is the large volume collapse to a close-packed structure at 11 GPa, near the semiconductor-to-metal transition.

In our calculations, we have used a modified version of the quotidian equation of state (QEOS). This equation-of-state model [16] is based on free energy construction which combines a Thomas-Fermi description for the free electron energy with a Cowan model for the ion free energy. Near solid density, the Barnes correction is applied to yield zero total pressure and the experimentally observed bulk modulus. This type of equation-of-state construction is naturally suited for two-temperature calculations since the electron and the ion components are treated separately.

Two modifications have been made to the standard QEOS model. The first is the splitting of the cold (zero Kelvin) isotherm into a high pressure and a low pressure phase joined together at a constant transition pressure of 11 GPa to coincide with the beginning of the sequence of structural phase changes and the transition to a metallic state. The low pressure isotherm is fitted to experimental data for density $\rho_0=2.3$ g/cm^3 and bulk modulus $B_0=98$ GPa. The high pressure phase is likewise fitted to static compression data which yields $\rho_0=3.84$ g/cm^3 and $B_0=0.68$ GPa extrapolated to zero pressure. The energy along the resulting piecewise continuous P-V curve is then obtained from the relation $E_c=-\int_{V_0}^{V} P\,dV$. The second modification concerns the bonding correction for expanded states by incorporating the experimentally known cohesive energy. This modification is described in detail in Ref. [17]. Its main effect is to provide a more accurate account of the expanded states occurring in the shock released material and does not affect the calculation of the shock compressed states.

Figure 1 shows the cold compression as well as the Hugoniot curves derived from our equation-of-state model. Also shown are data obtained from static [18,19] and shock compression [20,21] experiments. In our model, we cannot construct a cold compression curve to fit the static data and at the same time to yield a Hugoniot in agreement with the two shock measurements above 100 GPa. Given the precision and known accuracies of the static data, and the lack of reported uncertainties for the shock measurements in question, we have chosen to base our equation of state construction on the static compression measurements. However, the possibility remains that at high pressures our equation of state may render the material too compressible leading to over estimations of both the Hugoniot temperature and density. In any case, the accuracy in our calculated Hugoniot temperature is estimated to be better than 30%.

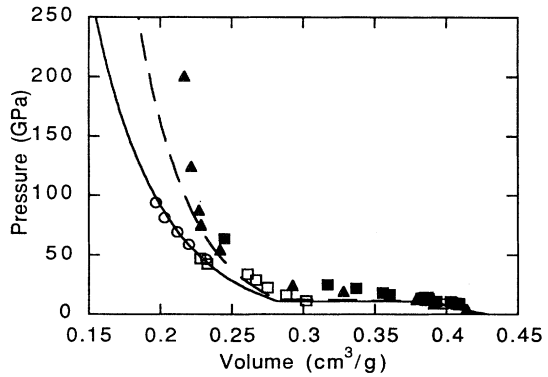

FIG. 1. Equation of state of silicon: (i) theoretical cold compression curve (solid line) and Hugoniot (dashed line), (ii) static compression data of Duclos, Vohra, and Ruoff (open circle) and Olijnk, Sikka, and Holzapfel (open square), and (iii) Hugoniot data of Gust and Royce (solid squares) and Pavlovskii (solid triangle).

The calculated Hugoniot parameters as well as the equation-of-state data corresponding to the shock state encountered in our experiment are detailed in Table I. For these cases, the cold compression contribution to the internal energy is small compared to the thermal energy component. This is because the large volume change in the isotherm occurs at a substantially lower pressure. Based on the Lindemann melting criterion [22] and high pressure melting data [23], our equation-of-state model yields a melting temperature of 5000–7000 K with a corresponding density of 5.5–6.5 g/cm^3. This implies that, at 5 to 10 times higher temperatures, the shock compressed state is a dense liquid. Liquid silicon is metallic with an electronic ionization state of 4. This leads to an ion-ion coupling parameter $\Gamma_{ii}=Z^2e^2/R_0kT_i$ (where $R_0=[3/4\pi n_i]^{1/3}$ is the ion sphere radius, Z the ionization state, and T_i the ion temperature) in excess of 40 for these shock states which can therefore be considered also as strongly coupled plasmas.

B. Electron-ion equilibration and electron thermal conduction in a shock wave

As pointed out earlier, the thermal energy in the shock front is carried initially by the ions. Part of this energy is transferred subsequently to the electrons via Coulomb collisions. Thermal equilibrium between electrons and ions can only be established somewhere behind the shock front. In addition to gaining energy from the ions, the colder electrons at the shock front will also be heated by the hotter electrons in the equilibrium region due to electron thermal conduction. To treat this problem, the fluid equations governing the conservation of mass, momentum and energy, written in flux conservation form, are as follows:

$$\frac{\partial\rho}{\partial t}=-\frac{\partial}{\partial x}(\rho u)\,, \tag{1}$$

$$\frac{\partial}{\partial t}(\rho u)=-\frac{\partial}{\partial x}(p_e+p_i+\rho u^2)\,, \tag{2}$$

$$\frac{\partial}{\partial t}(\rho E_e)=-\frac{\partial}{\partial x}\left[\rho u\left[E_e+\frac{p_e}{\rho}\right]-\kappa\frac{\partial T_e}{\partial x}\right]-g(T_e-T_i)\,, \tag{3}$$

TABLE I. Characteristics of the shock-produced plasmas. Γ_{ii} is the ion-ion coupling parameter.

Shock speed (10^6 cm/s)	Pressure (GPa)	Compression	n_i (10^{23} cm^{-3})	T_i (eV)	Γ_{ii}
1.5±0.1	300±50	2.4±0.05	1.17±0.02	2.4±0.8	76±25
1.8±0.2	460±100	2.6±0.15	1.28±0.07	3.7±1.4	51±19
2.0±0.1	600±90	2.7±0.10	1.34±0.05	4.7±1.5	40±13

$$\frac{\partial}{\partial t}\left[\rho E_i+\frac{\rho u^2}{2}\right]=-\frac{\partial}{\partial x}\left[\rho u\left[E_i+\frac{u^2}{2}+\frac{p_i}{\rho}\right]\right] +g(T_e-T_i)\ . \tag{4}$$

In contrast to a single-temperature calculation, the energy conservation equation is formulated separately for the electron and ion components. They are also described by separate equations of state: $p_j=p_j(\rho,E_j)$ and $T_j=T_j(\rho,E_j)$, where $j=e(i)$ for electrons (ions). Both components share a common mass density ρ and fluid velocity u.

The equilibration between the electrons and the ions is described by the electron-ion coupling constant g assuming that the rate of energy exchange is linearly dependent on the temperature difference. This is valid only when the latter is sufficiently small. In plasma physics, a more traditional description of thermal equilibration between electrons and ions is $dT_i/dt=(T_e-T_i)/\tau_{eq}$ where τ_{eq} is the equilibration time. This yields correspondingly $g=c_i/\tau_{eq}$ where c_i is the ion specific heat. For weakly coupled plasmas $c_i=3n_ik/2$ where k is the Boltzmann constant. For weakly coupled and nondegenerate plasmas, τ_{eq} is given by an expression due to Spitzer [24],

$$\tau_{eq}=\frac{3}{8\sqrt{2\pi}}\frac{m_ikT_e}{(Z^*)^3n_ie^4\ln\Lambda}\left[\frac{kT_e}{m_e}\right]^{1/2}, \tag{5}$$

where m_i is the ion mass, n_i the ion density, e the electron charge, Z^* the average ionization of the ions, and $\ln\Lambda$ the Coulomb logarithm. Accordingly, g exhibits a $T_e^{-3/2}$ dependence which arises from the velocity dependence of the scattering cross section in a Maxwellian plasma. An extension of the Spitzer formula for a degenerate plasma is given by Brysk [25],

$$\tau_{eq}=\frac{3\pi m_i\hbar^3}{8m^2(Z^*)^3e^4\ln\Lambda}[1+e^{-\mu/kT_e}]\ . \tag{6}$$

Here, $\hbar=h/2\pi$ where h is Planck's constant, and μ is the chemical potential. However both of these expressions for τ_{eq} are valid only for plasmas where the ion-ion correlation is weak. For strongly correlated systems, these plasma formulas underestimate the equilibration time and hence overestimate the coupling coefficient. For example, assuming $c_i=3n_ik/2$ and $\ln\Lambda=2$, Eqs. (6) yields a value of $g=3.2\times10^{19}$ W/m^{3}K for aluminum at STP. This is two to three orders of magnitude higher than the electron-phonon coupling constant observed in many metals [26–30]. Unfortunately, simple analytical expressions for g or τ_{eq} are not available for strongly coupled plasmas. In this work, g is left as a free parameter with a constant value.

Electron thermal conduction is governed by the thermal conductivity κ. In the absence of a two-temperature model, we have assumed that $\kappa(T_e,T_i)=\kappa_0(\theta)T_e/T_i$ where θ is the equilibrium Hugoniot temperature and $\kappa_0(\theta)$ is obtained from an equilibrium, dense plasma model of Lee and More [4]. This phenomenological approximation may be reasonable since for strongly coupled plasmas the electron-ion scattering rate depends mainly on the ion temperature through the ion structure factor and for degenerate electrons the heat capacity is a linear function of electron temperature. Although thermal conductivity calculations using the Lee and More model have not been verified experimentally, the model yields electrical conductivities of dense plasmas consistent with observations [1,31].

Figure 2 shows the calculated density and temperature profiles of a 460 GPa shock wave in silicon for $\kappa=3700$ W/m K and $g=10^{17}$ W/m^3 K. The difference in temperatures is the result of finite electron thermal conductivity and electron-ion energy exchange rate. It should also be noted that the jump in electron temperature at the shock front is driven by the electron heat flux.

C. Optical emission from a shock front

To model the measurement of optical emission from a shock front in flight in silicon, one needs to consider a layered structure consisting of the shock compressed ma-

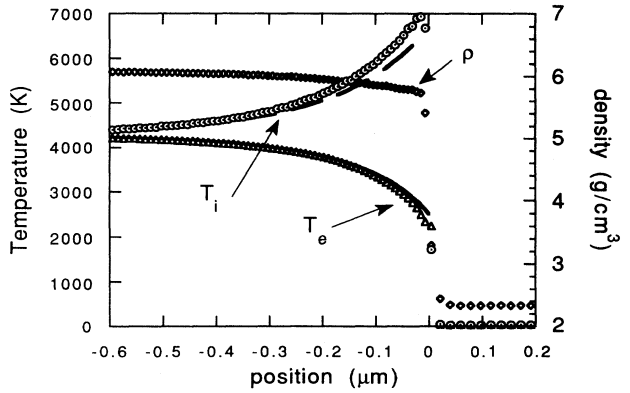

FIG. 2. Spatial profiles of ion temperature T_i (circle), electron temperature T_e (triangle), and density ρ (diamond) for a 460 GPa shock in silicon obtained from the numerical model and that of T_i (dashed line) and T_e (solid line) obtained from the analytical model.

terial, the intervening cold silicon layer, and the silicon-vacuum interface. We solve the Helmholtz equations [32] for an electromagnetic wave (at 430 nm or 570 nm) incident on the structure from the vacuum. The optical properties of the materials are represented by their corresponding dielectric functions. The calculation yields the absorption profiles of radiation in the various layers. The "observed" shock emission is then obtained by applying Kirchhoff's law and integrating over the entire absorption profile. This procedure automatically takes into account reflection at the shock front, absorption in the cold silicon layer, as well as thin-film interference effects produced by the silicon layer. To compile a temporal history of the "observed" shock emission, the calculation is repeated at various times as the shock wave moves through the silicon towards the vacuum interface and during the shock release. A similar method has been used earlier to model optical emission from shock released materials [17].

For the plasma in the shock wave region, its dielectric function is given by $\varepsilon(\omega)=I+i4\pi\sigma(\omega)/\omega$. The frequency-dependent electrical conductivity is obtained using the Drude model: $\sigma(\omega)=Z^*n_ie^2/[m_e(1/\tau_{ei}-i\omega)]$ where the electron-ion collision time τ_{ei} is related to the dc conductivity σ_0 via $\tau_{ei}=m_e\sigma_0/Z^*n_ie^2$. The average ionization Z^* is given by the Thomas-Fermi prescription. Nonequilibrium conductivity models have not been available. To take into account the two-temperature effects, we have assumed phenomenologically that $\sigma_0=\sigma_0(\rho,T_i)$ since the electron-ion scattering rate depends mainly on the ion temperature through the ion structure factor. The dense plasma model of Lee and More [4] is used for the calculation of σ_0. As pointed out earlier, this model has yielded electrical conductivities consistent with experimental observations [1,31].

For the thin layer of cold silicon between the shock front and the vacuum, its optical properties are described using experimental values of the dielectric constant of $(24.232+i1.937)$ at 430 nm and $(16.190+i0.254)$ at 570 nm [33].

Examples of the calculated shock emission are presented in Fig. 3. For all assumed values of the electron-ion coupling constant g, the intensity of the emission rises as the shock approaches the vacuum interface. The amplitude of the signal becomes increasingly more modulated, as a result of interference effects due to reflections between the shock front and the vacuum interface. The modulation period depends on the shock speed and the wavelength of the emission. On a time scale longer than the periods of these modulations, the intensity shows an exponential increase with $1/e$-folding times of about 14 ps at 430 nm and 90 ps at 570 nm. These rise times are governed by the absorption constant of cold silicon and the shock speed. The intensity of the optical emission reaches a maximum when the shock arrives at the vacuum interface. Then, it decreases rapidly as the shock releases into vacuum producing an optically thick region of expanded and colder material. The late time emission originates from the shock release plasma in the vicinity of the critical density layer. The calculation clearly indicates that the intensity of the shock emission is reduced

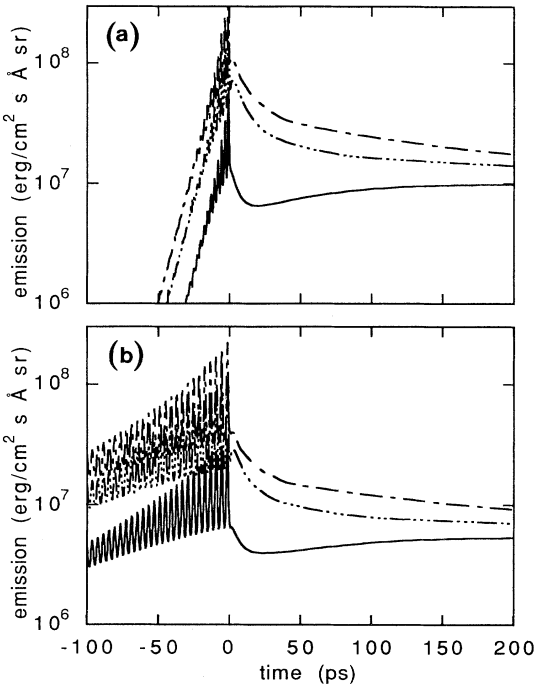

FIG. 3. Calculated intensities of emission at (a) 430 nm and (b) 570 nm from a 460 GPa shock wave for the equilibrium case using Lee and more conductivity (dot-dashed line), and for the nonequilibrium cases using Lee and More conductivity for g of 10^{17} W/m^3 K (dot-dot-dot-dashed line) and 10^{16} W/m^3 K (solid line).

with decreasing values of g, that is, lower rates of energy exchange between electrons and ions.

D. Ionization precursor

A common phenomenon associated with strong shocks in gases and rarefied plasmas is the formation of ionization waves in the cold material ahead of the shock front. Such waves may be driven by radiation or electron heat conduction. An analogous process may take place in silicon. This issue needs to be addressed since an ionization wave moving ahead of the shock front may screen the thermal radiation originating from the shock compressed material and lead to an apparent reduction of its brightness temperature.

For the shock pressures of interest here, simple calculations show that the visible and ultraviolet radiation flux produced at the shock front in the ionizing wavelength band of 200–1000 nm is insufficient to ionize silicon significantly, even assuming blackbody emissivities.

The free streaming of thermal electrons from the shock heated region will be limited to a range of the order of the Debye length which is comparable to a few lattice spacings. On the other hand we have also examined the possibility of an ionization wave driven by thermal conduction, in which ionization is treated by a rate equation containing terms for electron impact ionization and Auger three-body recombination [34]. In this model, a

steady wave solution is obtained from the continuity of thermal flux and temperature across the shock front. The results suggest that an ionization wave with electron temperatures in the range of 7000–10 000 K may be produced extending about 4 μm ahead of the shock front. However, the electron density is only about 10^{15} cm^{-3} even at the shock front, which is substantially lower than the critical densities corresponding to radiation at 430 nm or 570 nm. Such weak ionization has little effect on the optical properties of silicon in the wavelength range where the shock emission measurements are made.

III. EXPERIMENT

Figure 4 shows a schematic diagram of the experimental arrangement. A pulsed laser beam is focused onto the front surface of a slab target. Laser-driven ablation then drives a strong shock into the sample. As the shock wave approaches the free (rear) surface of the target, optical emission from the shock front is recorded by a streak camera (Hamamatsu C1370). The shock emission is collected with a 50 mm, f/1.4, Zeiss objective and relayed through a 600 mm achromat to form an image of the target rear surface on the entrance slit of the streak camera with a magnification of 12. Narrow-band (10 nm bandwidth) interference filters centered at 430 nm or 570 nm are placed at the slit. The spatial and temporal resolutions of the measurement are respectively 20 μm and 20 ps. The absolute response of the streak camera is calibration *in situ* prior to and also after the experiment using a tungsten filament heated to approximately 3200 K. To provide a time fudicial, a part of the incident laser beam is also directed onto a small region on one edge of the streak camera slit using an optical fiber. Other important experimental considerations are discussed below.

A. Laser irradiation conditions

In the experiment, a frequency-doubled Nd-glass laser beam providing a 2.3 ns full width at half maximum (FWHM) pulse at a wavelength of 0.5 μm is focused with a $f/2.2$ lens onto the front surface of an intrinsic $\langle 100 \rangle$ silicon wafer. The focal spot diameter is kept constant throughout the experiment while the laser irradiance on target is varied using neutral density filters.

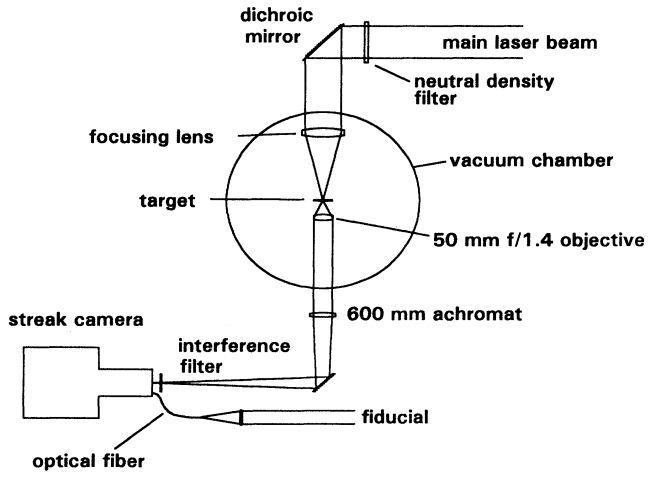

FIG. 4. Schematic diagram of the experimental setup.

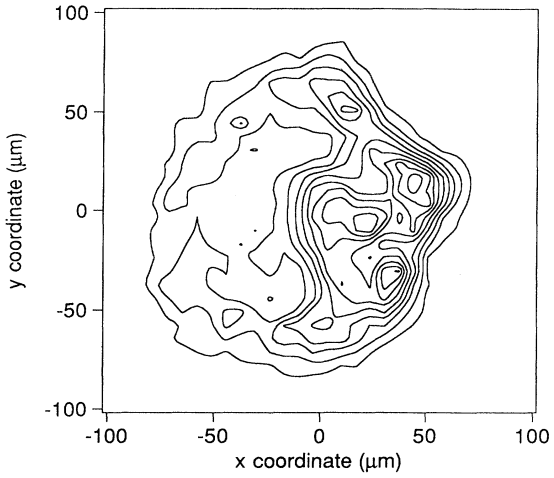

FIG. 5. An example of the time-integrated intensity distribution in the laser focal spot. Contours at 10% intervals.

Figure 5 shows a typical example of the time-integrated intensity distribution of the laser focal spot in vacuum. The spatial resolution of this measurement is about 5 μm. The laser beam is confined to a region of about 150 μm in diameter. Significant spatial modulations in the laser intensity are evident. These may cause nonuniform ablation of the target, giving rise to a nonuniform ablation-drive shock front. However, for the nanosecond laser pulse, lateral thermal transport may provide significant smoothing of the laser beam in the deposition region of the plasma. Moreover, the scale size of the laser intensity modulations in the vacuum is less than 20 μm. Nonuniformities in the shock front with a similar scale size are expected to be greatly reduced due to hydrodynamic smoothing after the shock has propagated through the target with a thickness greatly exceeding 20 μm. As indicated by the spatially resolved shock emission in Fig. 6, a reasonably uniform shock front is observed.

A more important aspect of the target irradiation condition is the overall spatial distribution of the laser intensity. The higher intensity on the axis produces an inherent curvature in the shock front. Thermal and hydrodynamic smoothing will reduce but not eradicate the curvature of the shock front as it propagates through the target. Consequently, as the shock wave emerges from the free surface of the target, the extent of the breakout region and hence the observed shock emission intensity will increase with time. This effect is evident in Fig. 6. Thus, in the measurement of shock emission, care must be taken to limit the observation to a central region of the shock front where the curvature effect is negligible. It should also be noted that the propagation distance of the shock front must be kept sufficiently short that the effect of edge rarefaction on the region of observation is small.

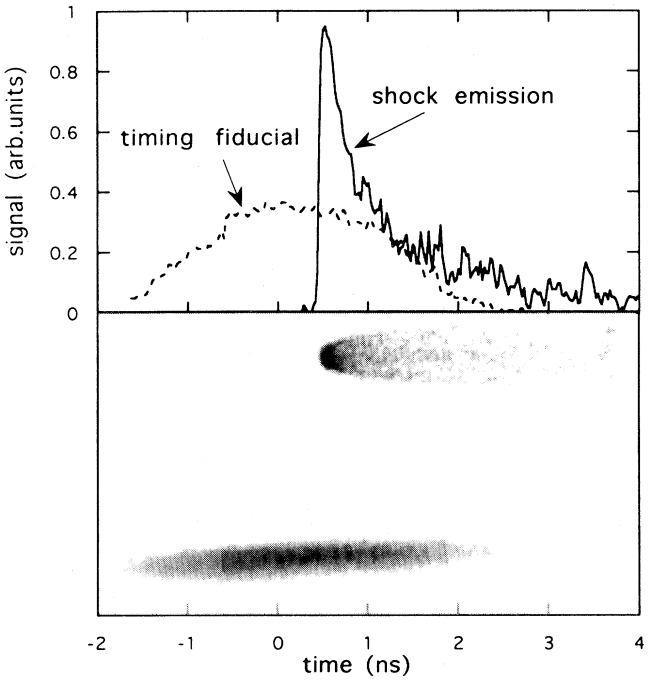

FIG. 6. Laser fiducial and shock emission: (upper panel) temporal history of intensity over a central 5-pixel region of the streak record, and (lower panel) steak camera record.

Apart from its effect on shock propagation, the nonuniform laser intensity distribution also renders it difficult to define the laser irradiance on target. We have arbitrarily defined an effective laser irradiance Φ_L as follows:

$$\Phi_L = 4E_L/(\tau_L \pi D_s^2) , \quad (7)$$

where E_L and τ_L are, respectively, the energy and duration (FWHM) of the laser pulse, and D_s is the width of the steady breakout region of the shock front as indicated in Fig. 6. The three different laser irradiation conditions used in this experiment are given in Table II. In general, D_s is less than 150 μm. This may be due to refraction of the focused laser beam in the plasma which expands in a nonplanar manner or other factors such as two-dimensional rarefaction.

B. Target material

Silicon is used as the target material in this study because of the unique advantage it offers. As a semiconductor with an indirect gap of 1.2 eV, silicon shows absorption coefficients [33] of 3.8×10^4 cm^{-1} and 6.5×10^3 cm^{-1} at wavelengths of 430 nm and 570 nm, respectively. The corresponding $1/e$-absorption lengths are 0.26 μm and 1.6 μm. For a dynamic range of about 80 which is typical of streak cameras with picosecond resolutions, even the shorter wavelength emission can be observed from a shock front when it is within 1 μm from the free surface of the target. For a shock speed of 2×10^6 cm/s, the apparent rise time of the emission signal will be about 50 ps which is readily resolvable. This renders it possible to observe the shock front in flight inside the solid, removing the usual difficulty where the shock front is visible only when it arrives at the free surface but is immediately obscured by the release of the surface [35]. The above estimate represents only the upper limit on how deep inside the solid the shock front becomes visible. A lower limit may be imposed by the intensity of the shock emission and the sensitivity of the streak camera. On the other hand, the viability of observing a shock front in flight can be greatly improved for measurements at longer wavelengths or at lower shock speeds.

Another equally important aspect of silicon is that its small band gap closes at a relatively low pressure of about 12 GPa. At the shock pressures of interest here (300–600 GPa), silicon is expected to be metallic with valence 4. Thus it can be considered as a dense plasma.

On the practical side, silicon also offers the advantage of ready availability as high-purity, ultrathin wafers with optical-quality surfaces.

TABLE II. Experimental conditions for the laser-generated shock waves.

D_s (μm)	Φ_L (10^{13} W/cm^2)	Φ_{sim} (10^{13} W/cm^2)	Shock speed (10^6 cm/s)
85±20	2.5±1.2	2.1±0.1	1.5±0.1
105±20	3.5±1.4	3.5±0.4	1.8±0.2
130±20	4.3±1.4	4.7±0.7	2.0±0.1

C. Shock-produced plasma

In this study, the dense plasma is produced in a solid by shock compression and the necessary strong shock is generated via laser-driven ablation of the solid. An advantage of shock-produced plasmas is that, if the shock condition is known, the plasma properties including density, temperature, and ionization can be deduced from a known equation of state. For laser-generated shock waves, the only parameter that can be directly measured to characterize the shock condition is the shock speed. To determine the shock speed, the shock transit times in targets of different thicknesses are compiled over repeated shots as presented in Fig. 7. The shock transit time is obtained by comparing the onset of shock emission to a time fiducial of the laser pulse (Fig. 6). These experimental data are compared with the results of one-dimensional (1D) hydrodynamic simulations [10]. The physics used in the numerical code includes inverse bremsstrahlung absorption of laser radiation, dense plasma conductivity [4], and a modified quotidian equation of state [16] as discussed in Sec. II. The calculations also assume thermodynamic equilibrium in the shocked material. In the simulations, the laser irradiances Φ_{sim} is used as a fitting parameter to yield shock transit times that are in agreement with observations (Fig. 7). For all cases, the values of Φ_{sim} are consistent with the measured effective laser irradiances Φ_L. This suggests that quasisteady, 1D shock waves are produced at depths of 68–85 μm. Accordingly, measurements of the shock emission are made on 68 μm thick silicon wafers. The shock speeds are obtained

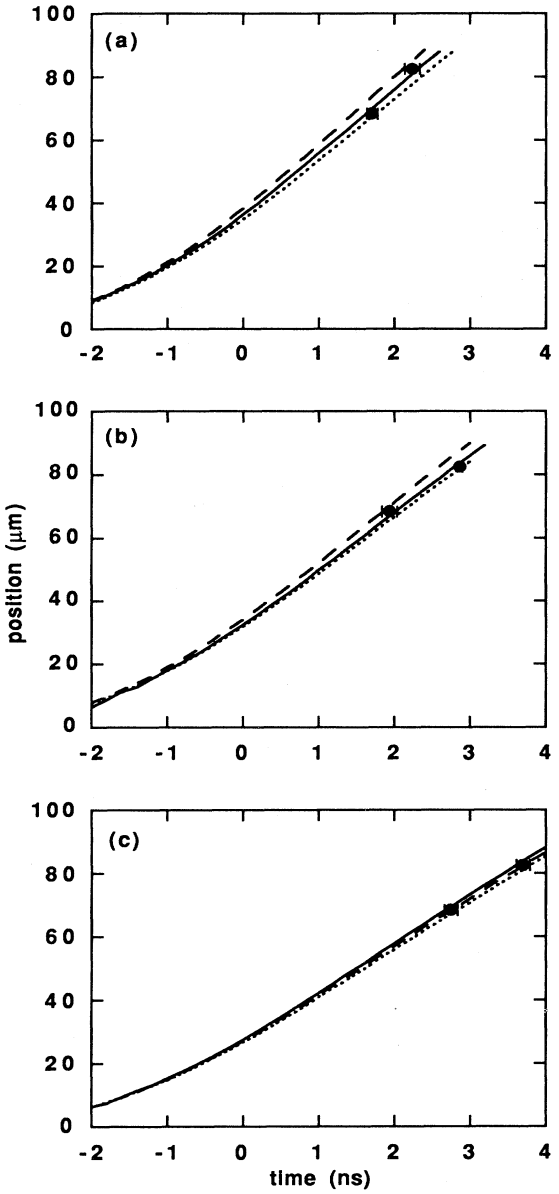

FIG. 7. Comparison of the observed shock transit times (solid circles) to calculated shock trajectories (solid line for the mean value of Φ_{sim}; dashed and dotted lines for the corresponding upper and lower bounds). (a) $\Phi_L=(4.3\pm1.4)\times10^{13}$ W/cm^2, $\Phi_{sim}=(4.7\pm0.7)\times10^{13}$ W/cm^2, (b) $\Phi_L=(3.5\pm1.4)\times10^{13}$ W/cm^2, $\Phi_{sim}=(3.5\pm0.4)\times10^{13}$ W/cm^2, and (c) $\Phi_L=(2.5\pm1.2)\times10^{13}$ W/cm^2, $\Phi_{sim}=(2.1\pm0.1)\times10^{13}$ W/cm^2.

from the simulations.

From these shock speeds and the silicon equation of state, the corresponding shock conditions and the parameters characterizing the shock-produced plasmas are obtained. The results have been presented in Table I. The very large ion-ion coupling constants are of particular interest in comparison to that existing in Jovian planets with $\Gamma_{ii}=20-50$ [36,37] and in the interiors of white dwarfs with $\Gamma_{ii}=10-200$ [38,39].

IV. INTERPRETATION OF THE SHOCK EMISSION DATA

The temporal history of the shock emission is obtained by averaging the signal over a central 20–40 μm region in the shock front. The results corresponding to a shock speed $u_s=2\times10^6$ cm/s are presented in Fig. 8. Each diagram displays an overlay of three shock emission signals. The shot-to-shot reproducibility of the data appears to be quite good. The much faster apparent rise time of the signals at the shorter wavelength is consistent with the stronger absorption of such radiation in the cold silicon ahead of the shock front. It is evident that the optical emission from the shock front becomes visible before it reaches the target free surface. Because of the finite temporal resolution (20 ps) of the streak camera, the rapid intensity modulations due to interference effects are not observed. To provide a proper comparison with data, the calculated emission intensity is convolved with a 20 ps FWHM Gaussian impulse response function. The results have been included in Fig. 8.

In the initial analysis, theoretical calculations are made assuming thermodynamic equilibrium in the shock front. A crucial parameter in the calculation is the electrical conductivity. For the purpose of comparison, both Spitzer conductivity [24] and a dense plasma conductivity [4] have been used. Since the shock state represents a

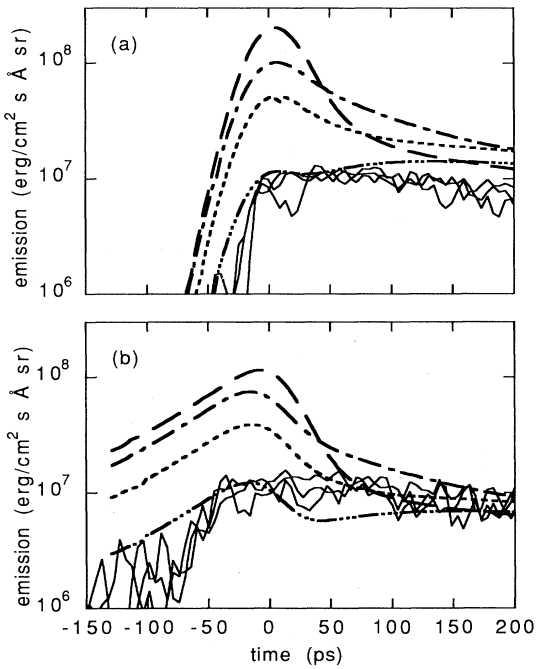

FIG. 8. Comparison of observed shock emission (solid line) at (a) 430 nm and (b) 570 nm with results of equilibrium calculations using Spitzer conductivity (dashed line) and Lee and More's conductivity (dot-dashed line), and nonequilibrium calculations using Lee and More conductivity for g of 10^{17} W/m^{3}K (dotted line) and 10^{16} W/m^{3}K (dot-dot-dot-dashed line). Error bars on the calculated results resulting from experimental and theoretical uncertainties are indicated. The magnitude of these combined uncertainties are listed in Table I.

strongly coupled plasma where simple treatment of electron-ion interactions by Debye screening is not expected to be valid, it is not surprising that calculations using Spitzer conductivity show strong disagreement with data (Fig. 8). However, the calculated intensities of shock emission remain a factor of 10 or more above the data even when the dense plasma conductivity is used.

Such a large discrepancy cannot be accounted for by the uncertainty (better than 30%) in the Hugoniot temperature derived from the theoretical equation of state or by the accuracy (within a factor of two) of electrical conductivity derived from a dense plasma model which has been shown to give satisfactory results in an earlier study on aluminum plasmas [1,31]. The next concern is whether the shock front is screened by a cooler, ionized region ahead of it. However, the possibility of an ionization precursor due to radiation or thermal conduction has been examined in Sec. II. Such processes appear to have negligible effects in the present experiment.

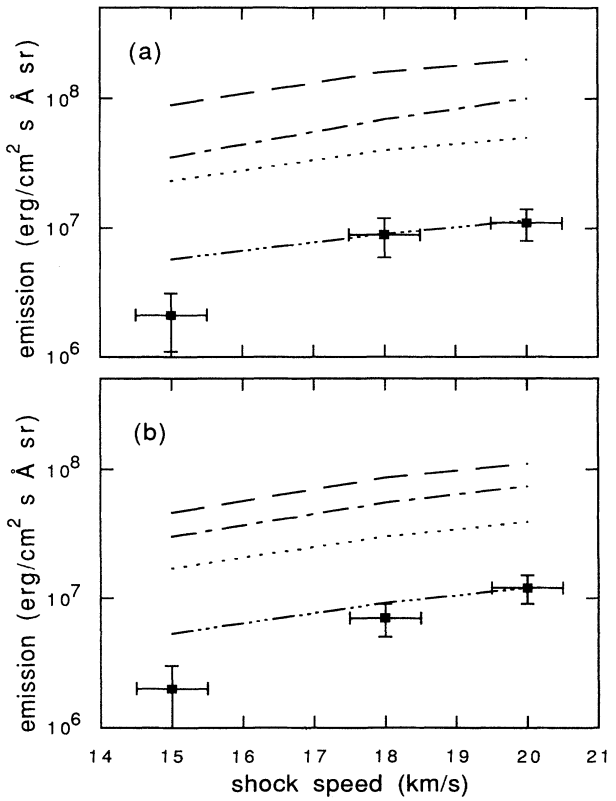

FIG. 9. Comparison of observed peak intensity of shock emission (solid square) at (a) 430 nm and (b) 570 nm with results of equilibrium calculations using Spitzer conductivity (dashed line) and Lee and More's conductivity (dot-dashed line), and nonequilibrium calculations using Lee and More's conductivity for g of 10^{17} W/m^3 K (dotted line) and 10^{16} W/m^3 K (dot-dot-dot-dashed line). Indicated on the emission calculation with the Spitzer conductivity are error bars resulting from combined experimental and theoretical uncertainties in the shock temperature. Similar uncertainties also apply to the three other calculated curves for the same reason, but are omitted in the diagram for clarity.

Alternatively, one may question the validity of the assumption of thermodynamic equilibrium at the shock front. Shock compression of the solid first leads to heating of the lattice or ions which then thermalize with electrons through Coulomb collisions. In regions far behind the shock front, complete thermodynamic equilibrium will be established when the time elapsed since the passage of the shock wave exceeds all equilibrium times. At the shock front, however, the temperature of the electrons may differ from that of the ions depending on electron thermal conduction and the rate of energy exchange between electrons and ions. As discussed in Sec. II, for finite values of electron thermal conductivity and electron-ion coupling constant, steep gradients in electron temperature will result in the shock wave. Consequently, radiation from the higher-temperature equilibrium region will be screened by the cooler electrons at the shock front. This would yield a lower observed electron temperature and hence a lower intensity in the observed optical emission.

The calculated intensities of shock emission assuming a constant and finite equilibrium rate between electrons and ions are presented in Fig. 8. Two different values of the electron-ion coupling coefficient are employed to illustrate its effect. The use of a constant coupling parameter over the range of temperatures and densities existing at the shock front may be unrealistic. Such an approximation becomes even more questionable in the released material where both the electron and ion densities drop rapidly. Thus, the interpretation of the experimental results should focus on the peak emission intensity at the time of shock breakout at the target free surface. The dependence of the peak intensity of the shock emission on shock speed is summarized in Fig. 9. The data suggest an electron-ion coupling coefficient of no greater than 10^{16} W/m^3 K. Weaker coupling may prevail in the case of the lowest shock strength.

V. DISCUSSION

A. The deduced value of g

Theoretical values of the electron-ion coupling constant under shock conditions are not known. Since silicon becomes metallic for shock amplitudes pertinent to this study, it may be instructive to examine existing findings on metals under normal conditions. Thermal relaxation in metals at normal densities has been investigated using ultrashort-pulse lasers which induce a transient population of hot electrons [26–30]. The subsequent thermalization of these electrons with the cold lattice is governed by the electron-phonon coupling coefficient. This process differs from a shock wave in that the electrons interact with phonons which are coupled modes of ion oscillations, rather than with individual ions. Moreover, the electrons are heated by the laser radiation while the background ions remain cold. Measurements based on surface reflectivity changes have yielded values of the electron-phonon coupling constant (in units of W/m^3 K) of $(5-10)\times10^{17}$ for tungsten [26], 10^{17} for copper [27] and gold [28], and 3.5×10^{16} for silver [30] whereas those

based on damage observations yielded lower values of 10^{16} W/m^{3}K for copper and 2×10^{16} W/m^{3}K for molybdenum [29]. It was argued that the damage criterion probed the bulk characteristics of the sample. The similar magnitudes of the electron-ion coupling constant in shocked silicon and the electron-phonon coupling constant in metals under normal conditions, and the extremely favorable comparison between the shock results to the damage-based results may be fortuitous. The finding is nonetheless intriguing given the disparity between the two phenomena.

It should also be noted that the ultrafast laser experiments indicate electron-ion scattering times of a few hundred femtoseconds. This is not to be confused with the electron-ion energy equilibration times which are of the order 250 ps in this experiment. The relatively long thermal relaxation time under shock conditions arises from the much larger electron heat capacity at high temperatures.

B. Electron-ion coupling and electron thermal conduction

In our numerical analysis, the electron-ion coupling constant g is treated as a constant, free parameter. However, the electron temperature gradient at the shock front is not determined independently by g. As illustrated in an analytical model, the details of which are described in the Appendix, the electron temperature at the shock front is dictated by a dimensionless parameter A defined as

$$A=\frac{\gamma^2\theta^2(u_s-u_p)^2}{\kappa_0 g}\ , \tag{8}$$

where γ is the electronic heat capacity temperature coefficient, θ is the Hugoniot temperature, u_s and u_p are, respectively, the shock and particle speed. Aside from a factor of ρ^2, the numerator in the expression for A is equal to the electron enthalpy flux per degree temperature rise required to bring the electrons to the equilibrium Hugoniot temperature. This quantity depends only on the equation of state. On the other hand, the denominator depends only on the transport properties through a combined effect of electron thermal conduction and electron-ion coupling in supplying the necessary enthalpy flux. For $A\ll1$, $T_e\sim T_i\sim\theta$. As A increases, T_e begins to diverge from T_i. This is illustrated in Fig. 10 for a shock wave at 460 GPa using different values of the product $\kappa_0 g$.

Accordingly, it is evident that experimental measurements of the electron temperature at the shock front can only be used to deduce the value of $\kappa_0 g$. Since both of these quantities are related to the fundamental process of electron-ion collision, they cannot be assigned values independently. A crucial improvement in future studies would be to assess experimental data on the electron temperature of a shock front using a model which can self-consistently provide the conductivities, the electron-ion coupling constant as well as equation-of-state parameters such as θ and γ.

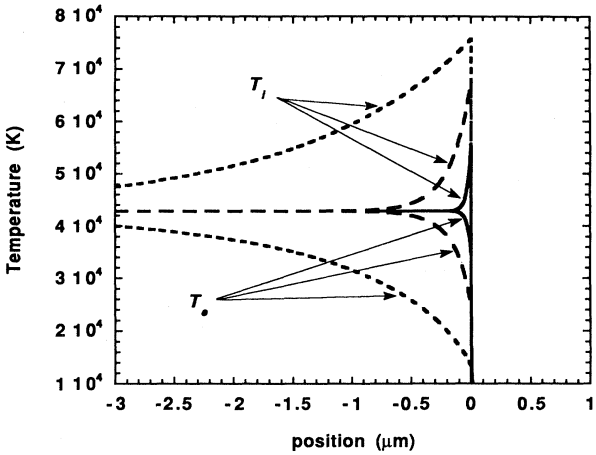

FIG. 10. Electron (T_e) and ion (T_i) temperature gradients in a 700 GPa shock wave for (i) $\kappa_0 g=3.7\times10^{19}$ W^2/m^{4}K^2, $A=0.5$ (dotted line), (ii) $\kappa_0 g=3.7\times10^{20}$ W^2/m^{4}K^2, $A=5$ (dashed line), and (iii) $\kappa_0 g=3.7\times10^{21}$ W^2/m^{4}K^2, $A=50$ (solid line).

C. Intensity modulation due to interference effects

Although the temporal resolution of our measurement is insufficient to resolve the predicted intensity modulation (Fig. 3) in the present study, the observation of this phenomenon would constitute an important test of a crucial assumption, namely, that the shock front can be treated as a Fresnel interface. Spatial structures at the shock front such as an ionization precursor will give rise to a refractive index gradient which can modify both the amplitude as well as the modulation depth in the intensity modulation. Such a test may be feasible for observations at a longer wavelength as well as a slower shock speed. The use of a much larger focal spot will also allow measurements to be made over a greater area of a planar shock front to increase the signal level. This will permit the use of streak cameras at a temporal resolution of 1–2 ps.

VI. CONCLUSIONS

The observation has revealed the important effect of thermal relaxation at the shock front. The existence of temperature gradients presents an ultimate obstacle to the determination of shock temperatures directly from pyrometric measurements of optical emission from a shock front. Care must be exercised in the interpretation of such data. The need to take into account of the nonequilbrium effects render the study of shock phenomena more complex. On the other hand, it offers an opportunity to assess qualitatively and quantitatively equilibration processes in shock states.

The study has yielded the first determination of the electron-ion coupling constant in a very strongly coupled plasma. The assumption of a constant equilibration rate throughout the entire gradients of temperature and density is questionable. The value of the constant obtained

should be considered as a density of temperature-averaged result. The seemingly good agreement with measured values of the electron-phonon coupling constant in metals may be fortuitous but it may also reflect the fundamental nature of Coulomb interactions in spite of the different asymmetry in electron and ion temperatures in a laser-heated metal and in a shock-produced plasma.

Finally, the need for self-consistent theoretical framework in modeling the equation of state, ionization, and transport coefficients of hot, dense matter is clearly accentuated by this investigation. The present piecemeal approach of deriving the different plasma properties from independent theoretical models has allowed us to extract some very useful information as a guide for further theoretical development.

ACKNOWLEDGMENTS

We wish to thank R. M. More and Y. T. Lee for many useful discussions. This work is supported by the Natural Sciences and Engineering Research Council of Canada.

APPENDIX

To elucidate how various processes affect the approach to equilibrium in a strong shock, a simple analytical model is used. In this model, the electrons gain energy via Coulomb collision with the ions and via electron thermal conduction. At constant volume and in the reference frame of the shock wave, the energy equations governing the two species are given by

$$c_e\frac{\partial T_e}{\partial t}=g(T_i-T_e)+\frac{\partial}{\partial x}\kappa(T_e,T_i)\frac{\partial}{\partial x}T_e\ , \tag{A1}$$

$$c_i\frac{\partial T_i}{\partial t}=g(T_e-T_i)\ . \tag{A2}$$

The electron heat capacity is taken to be $c_e=\gamma T_e$ as appropriate for a nearly Fermi-degenerate electron gas and γ is obtained form our equation-of-state model. As discussed earlier, the electron thermal conductivity in the shock region is described by a modified Sommerfeld model: $\kappa(T_e,T_i)=\kappa_0(\theta)T_e/T_i$ where θ is the Hugoniot temperature and κ_0 is obtained from an equilibrium, dense plasma model [4].

A complete description of the system requires the full set of fluid equations for the conservation of mass, momentum, and energy. This approach is only practical in numerical calculations. In omitting the continuity and momentum equations, we have assumed that the mass density and particle speed behind the shock front reach the Hugoniot values instantaneously. This is also evident from the omission of terms involving kinetic energy and $P\,dV$ work from the energy Eqs. (A1) and (A2). Instead, we require the sum of the electron and ion thermal energies to be constant everywhere in the shock wave, namely,

$$c_iT_i+\tfrac{1}{2}\gamma T_e^2=C_i\theta+\tfrac{1}{2}\gamma\theta^2=E_{\rm th}\ , \tag{A3}$$

where θ is the Hugoniot temperature and $E_{\rm th}$ is the thermal part of the internal energy imparted by the shock wave. It should be noted that numerical calculation using the full set of fluid equations show a maximum of 5% variations in the density, particle speed, and pressure from their Hugoniot values in the nonequilibrium region behind the shock front. However, the total thermal energy is constant to better than 2%.

By eliminating T_i from Eqs. (A1)–(A3), one arrives at a second-order partial differential equation in T_e,

$$\frac{\gamma T_e}{\kappa_0}\left[1+\frac{\gamma T_e}{c_i}\right]\frac{\partial T_e}{\partial t}=\frac{g\gamma T_e}{\kappa_0}\left[\frac{1}{c_i}+\frac{1}{\gamma T_e}\right]\left[\frac{\gamma}{2c_i}(\theta^2-T_e^2)+(\theta-T_e)\right]+\frac{c_i\theta+\gamma(\theta^2+T_e^2)/2}{[c_i\theta+\gamma(\theta^2-T_e^2)/2]^2}\left[\frac{\partial T_e}{\partial x}\right]^2+\frac{T_e}{[\theta+\gamma(\theta^2-T_e^2)/2c_i]}\frac{\partial^2T_e}{\partial x^2}\ . \tag{A4}$$

This equation must be solved in the moving frame of the shock front using a Galilean transformation. Here, the shock wave is taken to be propagating from right to left at a velocity $-u_s$. In the rest frame of the shock, unperturbed material flows into the shock front with a velocity $+u_s$ while the compressed material leaves with a slower velocity $v=u_s-u_p$ where u_p is the particle speed in the laboratory frame. We seek solutions to Eq. (A4) of the form $T_e=T_e(x+vt)=T_e(z)$. The problem can be rendered into a dimensionless form by defining two-dimensionless constants,

$$A=\frac{(\gamma v\theta)^2}{\kappa_0 g}\ ,\quad B=\frac{\gamma\theta}{c_i} \tag{A5}$$

and the following normalized parameters,

$$\tau=z\frac{g}{v\gamma\theta}\ ,\quad \xi=\frac{T_e}{\theta}\ ,\quad \eta=\frac{\gamma v}{g}\frac{dT_e}{dz}\ . \tag{A6}$$

Under a Galilean transformation and this change of variables, Eq. (A4) can be written in a dimensionless form as a pair of coupled first-order ordinary differential equations,

$$\frac{d\xi}{d\tau}=\eta\ , \tag{A7a}$$

$$\xi\frac{d\eta}{d\tau}=A\left[1+\frac{B}{2}(1-\xi^2)\right](1+B\xi)\times\left[\eta\xi+\xi-1-\frac{B(1-\xi^2)}{2}\right]-\left[\frac{1+B(1+\xi^2)/2}{1+B(1-\xi^2)/2}\right]\eta^2\ . \tag{A7b}$$

The point $\eta=0$, $\xi=1$ is a fixed point of these equations, corresponding to equilibrium behind the shock front.

These equations are integrated numerically using a standard fourth-order Runge-Kutta algorithm. As the initial condition, we set $\eta=0$ and $\xi=1.0-\varepsilon$ where $\varepsilon=10^{-12}$. The integration proceeds along τ.

The end point of the integration is determined by a jump condition at the shock front. The latter is obtained by considering Eqs. (3) and (4) for the electron and ion energies in the two-temperature fluid model. Integration over a vanishingly small volume element across the shock front yields

$$\rho_0 u_0\left[E_{e0}+\frac{p_{e0}}{\rho_0}\right]-\left[\kappa\frac{\partial T_e}{\partial x}\right]_0=\rho_1 u_1\left[E_{e1}+\frac{p_{e1}}{\rho_1}\right]-\left[\kappa\frac{\partial T_e}{\partial x}\right]_1, \quad \text{(A8)}$$

$$E_{i0}+\frac{u_0^2}{2}+\frac{p_{i0}}{\rho_0}=E_{i_i}+\frac{u_1^2}{2}+\frac{p_{i1}}{\rho_1}, \quad \text{(A9)}$$

where the subscripts 0 and 1 denote, respectively, the regions immediately ahead of and behind the shock front. In the unperturbed region, the electron enthalpy (E_e+p_e/ρ) and the thermal conductivity are negligible compared with those in the shocked region so that Eq. (A8) becomes

$$\rho u_1\left[E_{e_1}+\frac{p_{e_1}}{\rho_1}\right]=\left[\kappa\frac{\partial T_e}{\partial x}\right]_1, \quad \text{(A10)}$$

which states that the electron enthalpy flux at the shock front is balanced by the heat flux. Recognizing that $u_1=v$ in our coordinate system and that the electron enthalpy is well approximated by $\gamma T_e^2/2\rho$ for a degenerate, nearly free electron metal, Eq. (A10) can be rewritten in a dimensionless form giving

$$A\xi^2-\eta=0 . \quad \text{(A11)}$$

For the region behind the shock front, $A\xi^2>\eta$. The integration proceeds until Eq. (A11) is satisfied. This yields the complete temperature profiles. A result of this simplified analytical model is presented in Fig. 2 in comparison with that obtained from hydrodynamic simulations. The agreement is generally within 5%.

An interesting finding of this analytical model is that the electron temperature at the shock front is governed by the parameter A, the physical meaning of which has been discussed in Sec. V. This is also illustrated in Fig. 10. On the other hand, the shape of the temperature profile is determined by the parameter B which is a property of the equation of state only, as indicated in Eq. (A5).

[1] A. Ng, D. Parfeniuk, P. Celliers, L. Da Silva, R. M. More, and Y. T. Lee, Phys. Rev. Lett. **57**, 1595 (1986).

[2] H. M. Milchberg, R. R. Freeman, S. C. Davey, and R. M. More, Phys. Rev. Lett. **61**, 2364 (1988).

[3] R. Fedosejevs, R. Ottmann, R. Sigel, G. Kuhnle, S. Szatmar, and F. R. Schafer, Phys. Rev. Lett. **64**, 1250 (1990).

[4] Y. T. Lee and R. M. More, Phys. Fluids **27**, 1273 (1984).

[5] R. Cauble, R. J. Rogers, and W. Rozmus, in *Femotsecond to Nanosecond High Intensity Lasers and Applications,* SPIE Proceedings Vol. 1229 (SPIE, Bellingham, WA, 1990), p. 221.

[6] M. W. C. Dharma-wardana and F. Perrot, Phys. Lett. A **163**, 223 (1992).

[7] L. Da Silva, A. Ng, B. K. Godwal, G. Chiu, F. Cottet, M. C. Richardson, P. A. Jaanimagi, and Y. T. Lee, Phys. Rev. Lett. **62**, 1623 (1989).

[8] F. Perrot and M. W. C. Dharma-wardana, Phys. Rev. Lett. **71**, 797 (1993).

[9] P. Celliers, A. Ng, G. Xu, and A. Forsman, Phys. Rev. Lett. **68**, 2305 (1992).

[10] P. Celliers, Ph.D. thesis, University of British Columbia, 1988 (unpublished).

[11] S. Minomura and H. G. Drickamer, J. Phys. Chem. Solids **23**, 451 (1962).

[12] T. J. Dyuzheva, S. S. Kabalkina, and U. P. Novichvok, Sov. Phys. JETP **47**, 931 (1978); J. C. Jamieson, Science **139**, 762 (1963); A. Werner, J. A. Sanjurjo, and M. Cardona, Solid State Commun. **44**, 155 (1982).

[13] J. Z. Hu, L. D. Merkle, C. S. Menoni, and I. L. Spain, Phys. Rev. B **34**, 4679 (1986).

[14] H. Olijnyk, S. K. Sikka, and W. B. Holzapfel, Phys. Lett. **103A**, 137 (1984).

[15] S. J. Duclos, Y. H. Vohra, and A. L. Ruoff, Phys. Rev. Lett. **58**, 775 (1987).

[16] R. M. More, K. H. Warren, D. A. Young, and G. B. Zimmerman, Phys. Fluids **31**, 3059 (1988).

[17] P. Celliers and A. Ng, Phys. Rev. E **47**, 3547 (1993).

[18] H. Olijnyk, S. K Sikka, and W. B. Holzapfel, Phys. Lett. **103A**, 137 (1984).

[19] S. J. Duclos, Y. H. Vohra, and A. L Ruoff, Phys. Rev. Lett. **58**, 775 (1987).

[20] M. N. Pavlovskii, Fiz. Tverd. Tela (Leningrad) **9**, 3192 (1967) [Sov. Phys. Solid State **9**, 2514 (1968)].

[21] W. H. Gust and E. B. Royce, J. Appl. Phys. **42**, 1897 (1971).

[22] J. M. Ziman, *Principles of the Theory of Solids,* 2nd ed. (Cambridge University Press, Cambridge, 1972), p. 65.

[23] F. P. Bundy, J. Chem. Phys. **41**, 3809 (1964).

[24] L. Spitzer, *Physics of Fully Ionized Gases* (Interscience, New York, 1962).

[25] H. Brysk, Plasma Phys. **16**, 927 (1974).

[26] L. G. Fujimoto, J. M. Liu, E. P. Ippen, and N. Bloembergen, Phys. Rev. Lett. **57**, 1595 (1986).

[27] H. E. Elsayed-Ali, T. B. Norris, M. A. Pessot, and G. A. Mourou, Phys. Rev. Lett. **58**, 1212 (1987).

[28] R. W. Schoenlein, W. Z. Lin, J. G. Fujimoto, and G. L. Eesley, Phys. Rev. Lett. **58**, 1680 (1988).

[29] P. B. Corkum, F. Brunel, N. K. Sherman, and T. Srinivasan-Rao, Phys. Rev. Lett. **61**, 2886 (1988).

[30] R. H. M. Groenveld, R. Sprik, and A. Lagendijk, Phys. Rev. Lett. **64**, 784 (1990).

[31] A. Ng, P. Celliers, A. Forsman, R. M. More, Y. T. Lee, F. Perrot, M. W. C. Dharma-wardana, and G. A. Rinker, Phys. Rev. Lett. **72**, 3351 (1994).

[32] M. Born and E. Wolf, *Principles of Optics* (Pergamon, Oxford, 1980), p. 51.
[33] D. F. Edwards, *Handbook of Optical Constants of Solids,* edited by E. D. Palik (Academic, New York, 1985), p. 547.
[34] K. G. Svantesson and N. G. Nilsson, J. Phys. C **12**, 5111 (1979).
[35] Ya. B. Zel'dovich and Yu. P. Razier, *Physics of Shock and High Temperature Hydrodynamic Phenomena* (Academic, New York, 1966), Vol. I, p. 49.
[36] E. E. Salpeter, Astrophys. J. Lett. L **83**, 181 (1973).
[37] H. C. Graboske, J. B. Pollack, A. S. Grosman, and R. J. Olness, Astrophys. J. **199**, 265 (1975).
[38] E. Schatzman, *White Dwarfs* (White-Holland, Amsterdam, 1958).
[39] H. M. van Horn, J. Phys. (Paris) Suppl. **41**, C2-97 (1980).